PAPER

Visible light metasurface for adaptive photodetection

To cite this article: Ataollah Kalantari Osgouei *et al* 2022 *J. Phys. D: Appl. Phys.* **55** 475103

IOP Publishing Journal of Physics D: Applied Physics
J. Phys. D: Appl. Phys. **55** (2022) 475103 (8pp) https://doi.org/10.1088/1361-6463/ac90d0

Visible light metasurface for adaptive photodetection

Ataollah Kalantari Osgouei[1,2,*], Amir Ghobadi[1,3], Bahram Khalichi[1,3], Rana Asgari Sabet[4], Onur Tokel[2,4] and Ekmel Ozbay[1,2,3,4,*]

[1] NANOTAM-Nanotechnology Research Center, Bilkent University, 06800 Ankara, Turkey
[2] Department of Physics, Bilkent University, 06800 Ankara, Turkey
[3] Department of Electrical and Electronics Engineering, Bilkent University, 06800 Ankara, Turkey
[4] UNAM-Institute of Materials Science and Nanotechnology, Bilkent University, Ankara, Turkey

E-mail: akalantari@bilkent.edu.tr and ozbay@bilkent.edu.tr

Received 23 July 2022, revised 22 August 2022
Accepted for publication 9 September 2022
Published 5 October 2022

Abstract

Semiconductor-based sub-wavelength metasurfaces are promising device platforms for the realization of optically thick and electrically thin photodetectors. Strong light–matter interactions in ultrathin film regions provide an opportunity to achieve near-unity absorption in dimensions comparable with carrier diffusion length and this, in turn, leads to an efficient collection of photogenerated carriers. Moreover, the use of phase change materials can provide real-time active tuning of optical responses of metasurface-based devices. In the first part of this paper, a tunable color filtering device is demonstrated using a metasurface design made of sub-wavelength antimony trisulphide (Sb_2S_3) grating placed on top of a continuous silver layer. Four distinct optical states can be acquired upon (a) the changes in the incident light polarization and (b) the phase transitions of Sb_2S_3. Numerical simulations and theoretical modeling data show that Fabry–Perot resonances are the driving phenomena when the proposed design is normally illuminated by an electromagnetic field with transverse electric polarization. In contrast, surface plasmon resonances are excited in transverse magnetic polarization. Furthermore, it is shown that the resonance wavelengths of the proposed design can be dynamically tuned using the geometrical parameters. Later, in the second part of the paper, adaptive photodetection is designed by integrating a 5 nm Sb_2S_3 layer as a collection layer into the structure. The proposed metasurface design provides light–matter interaction in the Sb_2S_3 layer and maximizes the photogenerated carriers' collection efficiency. The optically thick and electrically thin adaptive photodetection offers an opportunity to design efficient active optoelectronic and photonic devices.

Keywords: semiconductor-based metasurfaces, tunable color filter, phase change materials, adaptive photodetection

(Some figures may appear in colour only in the online journal)

1. Introduction

Metasurfaces are artificial composite structures that are designed to manipulate light–matter interactions at the sub-wavelength scale [1–3] to achieve different properties such as light absorption [4, 5], asymmetric light transmission [6, 7], negative refractive index [8, 9], and polarization conversion [10, 11]. One of the most extensively explored areas in recent years has been the concept of perfect light absorbers (PLAs). Metasurfaces-based PLAs can reach near-unity absorptivity at specific wavelength ranges. These structures are widely used for various optoelectronic applications including optical filters [12, 13], photodetectors [14, 15],

* Authors to whom any correspondence should be addressed.

and solar cells [16, 17]. In principle, semiconductors are the main building blocks of photodetection technology, and various designs such as quantum dots [18], resonant cavities [19], and two-dimensional (2D) materials [20] are utilized for this purpose. However, semiconductors have non-resonant light absorption and harvest photons non-selectively with energies above their band gap. In the meantime, phase-change materials (PCMs) based metasurfaces have the ability to achieve dynamically tunable light absorption due to their optical properties that can be modified by applying an external stimulus [21, 22]. The main advantages of PCM-based metasurfaces over other designs originate from their unique electrical and optical features, including wavelength selectivity, high thermal durability, fast phase transitions, and possible fabrication technology. As a result, the integration of PCM-based metasurfaces with semiconductors can provide us an opportunity to design adaptive photodetectors with exceptional properties. Nevertheless, PCMs have been rarely utilized for photodetection applications. Among all PCMs, germanium–antimony–tellurium ($Ge_2Sb_2Te_5$) and vanadium dioxide (VO_2) have the unique property of being visible responsive semiconductors [23, 24]. Therefore, the metasurfaces made of these materials can have potential applications in active visible light photodetection. However, these structures can suffer from high absorption loss within the visible spectrum, resulting in low-quality factor absorption resonance (low-Q).

In the first part of the paper, we demonstrate a semiconductor-based metasurface absorber consisting of antimony trisulphide (Sb_2S_3) nanograting with low absorption loss and wide bandgap, placed over a metallic reflector to create a multiple color filter within the visible range. In contrast to the insulator to the metal transition of VO_2, which requires a constant flow of energy to maintain a structural state, the transition of Sb_2S_3 from the amorphous to the crystalline state is stable at room temperature. In other words, the crystallization of Sb_2S_3 can be achieved by increasing the temperature of the material to form the crystal formation either by using optical or electrical pulses with a duration of nanoseconds or generally by heating the entire sample. Conversely, the transition from crystalline to the amorphous state of the material can be achieved by using a short period of high-intensity laser pulses to randomize the atomic arrangement of the structure, along with rapid cooling to prevent the material from recrystallizing [25, 26]. Using finite-difference time-domain simulation as a numerical analysis approach [27], it is shown that two different colors are successfully achieved for each two orthogonal polarization modes of the incident light. In total, the proposed semiconductor-based metasurface can generate four distinct colors for four different states made through the phase transitions of Sb_2S_3 and polarization changes of the incident light. Moreover, the electric and magnetic field distributions at the resonance wavelengths of the proposed metasurface absorber indicate that Fabry–Perot (FP) resonances are excited in transverse electric (TE) mode, while surface plasmon resonances are deriving phenomena in transverse magnetic (TM) mode. Later, in the second part of the paper, we integrate a thin layer of Sb_2S_3 with a 5 nm thickness into the semiconductor-based metasurface absorber to convert the filtering design into a dynamically tunable photodetector in the visible range. The sub-wavelength thickness of the design, besides its near unity absorption in the visible range (due to the strong light–matter interactions), leads to the efficient harvesting and collection of photogenerated carriers. The photocurrent response of the design in the visible region is numerically analyzed by utilizing COMSOL Multiphysics [28], a finite-element-based method solver, in order to demonstrate its spectrally selective photodetection capability.

2. A dynamically tunable color filter design

2.1. Design, simulation, and results

As mentioned, Sb_2S_3 reveals distinct refractive index (n) and extinction coefficient (k) spectral responses at amorphous and crystalline states. According to figure 1(a), it is seen that the crystalline state of Sb_2S_3 has a higher refractive index than that of the amorphous state across the whole spectrum. While the amorphous state has an absorption response in the visible range, upon phase transition, the optical band gap gets narrower (a red-shift in the k spectral edge), and a near-infrared (NIR) responsive optical device can be obtained. Therefore, an Sb_2S_3-based metasurface absorber can cover a wide range of optical regions from ultraviolet to NIR. However, a metasurface-based design architecture needs to be developed to achieve this goal. The schematic of the proposed Sb_2S_3-based tunable color filter metasurface is shown in figure 1(b), where nanograting Sb_2S_3 is placed on top of a continuous metallic reflector. Silver (Ag) is used as a metal material with the frequency-dependent refractive index taken from the Johnson and Christy model database [29]. Moreover, the frequency-dependent refractive indices of Sb_2S_3 for both amorphous and crystalline states (as shown in figure 1(a)) are taken from [25, 26]. As a result of numerical optimizations, the optimal design geometries are found to be $t = 21$ nm, and $w = 180$ nm, while $p = 280$ nm is the optimal period of the unit cell of the structure. Furthermore, the thickness of the bottom Ag layer is sufficiently thick enough to suppress the transmission in our desired ranges. To explore the absorption behavior, the proposed structure is normally illuminated by the TE and TM polarized uniform plane waves propagating along $-y$ direction at both amorphous and crystalline states. The obtained spectral profiles are shown in figure 1(c). As this figure implies, we have four apparent states annotated as: (a) TE Amos., (b) TE Crys., (c) TM Amos., and (d) TM Crys. The absorption responses and the corresponding spectral positions of the resonances are different from each other for all possible states of the proposed metasurface. Each state covers a specific spectral range in the visible range, and consequently, it has its own specific color. Based on the data shown in figure 1(c), the absorption peak shifts from 475 nm to 582 nm for the TE polarization upon the phase change from amorphous to crystalline state. For the TM polarization case, the resonance wavelength experiences a shift from 545 nm to 650 nm upon a similar phase transition. The obtained results confirm that the

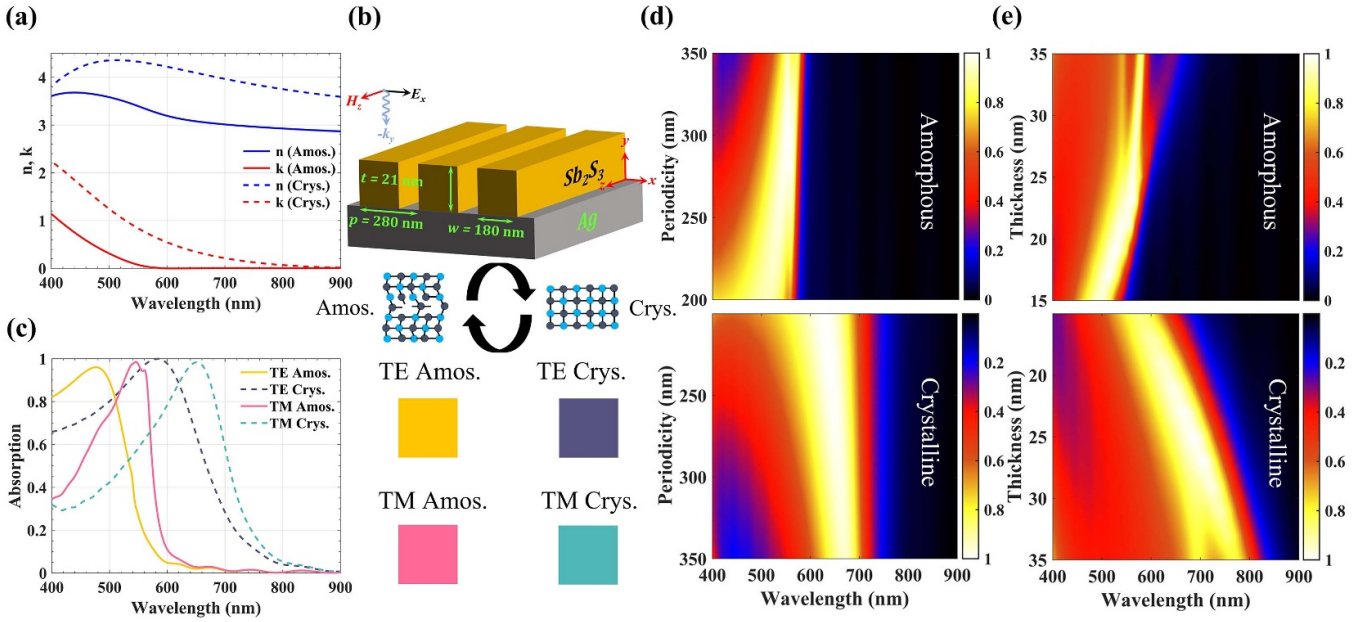

Figure 1. (a) The real and imaginary components of the refractive indices of Sb_2S_3 at the amorphous (Amos.) and crystalline (Crys.) states. (b) Schematic representation of the proposed Sb_2S_3-based tunable color filter metasurface absorber. (c) The simulated absorption spectra and the corresponding calculated D65 illumination data at different phase states and polarization modes, demonstrating the proposed structure's color variations. All results are obtained when the structure is normally illuminated by TE ($z-$) or TM ($x-$) polarized incident waves. Four different visible light colors are generated and recognized at the reflective mode of the structure as forsythia, French pink, aurora splendor, and crystalsong blue for TE Amos., TM Amos., TE Crys., and TM Crys., respectively. (d) The simulated counterplot of absorptivity as a function of wavelength for different periodicities (p) (while keeping the grating dimensions at their optimal values) at amorphous and crystalline states and (e) the simulated counterplots of absorptivity versus wavelength for different thicknesses of the Sb_2S_3 nanograting (t) (while keeping the design's periodicity and width of the nanograting at their optimal values) at amorphous and crystalline states for the TM polarization mode.

proposed metasurface could dynamically generate four different colors. To better understand the actual colors of the proposed metasurface, the corresponding color-switching of the reflection spectra (reflection $= 1-$ absorption) is calculated by the D65 illuminations method defined by the International Commission on Illumination [30]. The D65 illumination data can represent the structural colors' variations upon the phase transitions and the polarization mode changes. Indeed, the proposed metasurface generates four different visible light colors recognized at the reflective mode of the structure as forsythia, French pink, aurora splendor, and crystalsong blue for TE Amos., TM Amos., TE Crys., and TM Crys., respectively. In addition, the resonance wavelengths of the design can be passively tuned using the geometrical parameters to acquire near-perfect light absorption in a specific wavelength range within the visible spectrum. This can be seen in the 2D contour plots of the absorption as a function of changes in the periodicity (p) and thickness (t), plotted in figures 1(d) and (e) for the TM polarization mode. Based on these plots, increasing the periodicity (while keeping the grating geometries at their optimal values) induces a smooth red-shift in the absorption peak and leads to a narrower full-width-at-half-maximum. The grating height monolithically shifts the peak toward longer wavelengths, almost keeping the spectral shape. While the proposed design in the amorphous state operates at the shorter visible range, the crystalline state provides operation in the long visible and NIR ranges. Therefore, the proposed design is a dynamically tunable reflective color filter, and it can also be developed to operate as an adaptive photodetector by considering the semiconducting nature of Sb_2S_3. However, this requires knowledge of the involved absorption mechanisms and the role of each layer in the light-harvesting.

2.2. Physical mechanism

To understand the physical behavior of the tunable property of the proposed metasurface-based color filter, the magnetic (H-field) and electric (E-field) field distributions are simulated at the resonance wavelengths for both TM and TE polarizations, as shown in figures 2(b)–(e). The view plane is also schematically shown in figure 2(a). As plotted in figures 2(b) and (c), both E-field and H-field show the formation of hot spots in the metal–dielectric interface, resembling the excitation of localized surface plasmon resonance (LSPR) modes. Generally, it is possible to excite LSPR modes in a metal–dielectric interface using a diffraction grating. In this scenario, the resonance wavelength (λ_{res}) can be expressed as:

$$\lambda_{res} = \mp \frac{p}{m} \sqrt{\frac{\varepsilon_{metal} . n_{eff}^2}{\varepsilon_{metal} + n_{eff}^2}}, \qquad (1)$$

where p is periodicity, m is the diffraction order, and n_{eff} is the effective refractive index of the LSPR mode (which is a value

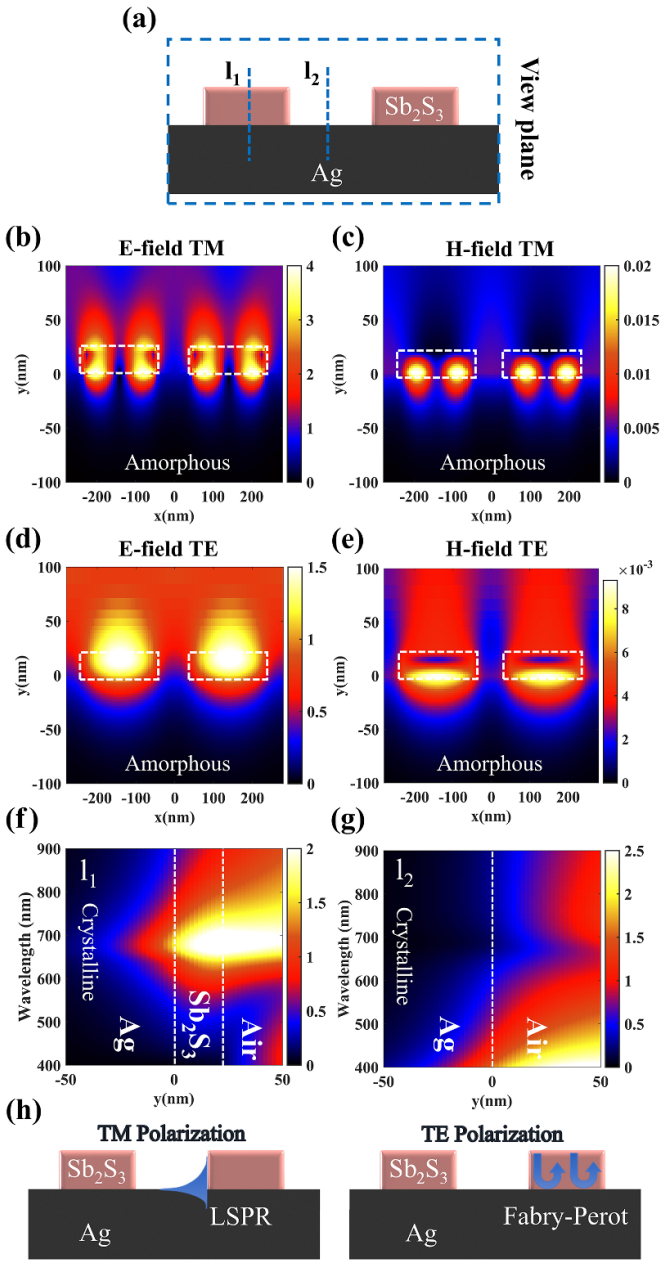

Figure 2. (a) The schematic representation of the proposed adaptive design when the electric field monitors are located at two different locations. The absolute value of the electric and magnetic mode profiles at the resonance wavelengths of (b) TM Amos. (*E*-field), (c) TM Amos. (*H*-field), (d) TE Amos. (*E*-field), and (e) TE Amos. (*H*-field), where the dashed white lines represent the Sb_2S_3 regions. The measured electric field amplitudes when the electric field monitors are located through (f) the center and (g) between the nanogratings for the TM polarized incident wave at the resonance wavelength of the crystalline state. (h) The schematic of the proposed adaptive structure indicates the physical mechanism behind the design for the TM and TE polarization modes.

between air and the grating index). Assuming $\varepsilon_{\text{metal}} \gg n_{\text{eff}}^2$, which is the case in our operation range, the formula can be simplified to $\lambda_{\text{res}} = \frac{p}{m} n_{\text{eff}}$. On the other side, n_{eff} is directly proportional to the refractive index of the grating material. This means that upon the phase transition from the crystalline to the amorphous state, the resonance wavelengths of the proposed structure can experience a shift. Specifically, for the TM polarization incident wave, the amorphous-crystalline transition causes a change in the grating refractive index and the resonance matching condition, which consequently leads to the resonance red-shift. Moreover, due to the formation of the LSPR mode, light can be confined inside the ultrathin Sb_2S_3 grating and near-unity light absorption in deep sub-wavelength dimensions can be obtained. This confinement can be seen from the line *E*-field spectral responses shown in figures 2(f) and (g). At the LSPR wavelength, the light is significantly enhanced near the reflector and inside the grating, while in the other wavelength values, the *E*-field contour plot resembles a metallic reflector. Considering the TE polarization incident wave, it can be understood that standing waves are formed across the light illumination direction instead of hot spots. These standing waves prove the excitation of the FP modes, and the change in grating index tunes the impedance matching condition. In other words, the ideal refractive index for near-unity absorption moves to another spectral range upon phase transition. All in all, the responsible absorption mechanism for TM polarization is LSPR, while FP modes drive near-unity light harvesting in the TE excitation, as shown in figure 2(h). Therefore, finding the permittivity of a hypothetical ideal absorber (HIA) over a reflector (see figure 3(a)) and comparing it with that of Sb_2S_3 can elucidate the peak resonance shift. For this aim, a modeling approach based on the transfer matrix method (TMM) is developed [31], and the reflection spectrum of the design is calculated by assuming that the structure is bounded by air. By considering a TM polarized incident wave propagating along the $-y$ direction with a $z-$ component, the magnetic field can be expressed as:

$$H_z(y) = \begin{cases} A_i e^{+ik_a(y-D_s)} + A_r e^{-ik_a(y-D_s)} & y > D_s \\ S_1 e^{+ik_s y} + S_2 e^{-ik_s y} & 0 < y < D_s \\ M_1 e^{+ik_m y} + M_2 e^{-ik_m y} & -D_m < y < 0 \end{cases}. \tag{2}$$

Next, by applying the appropriate boundary conditions, the reflection of the incident light from the proposed design can be obtained as $R = |F_{21}/F_{11}|^2$. Here, $F = \begin{bmatrix} F_{11} \\ F_{12} \end{bmatrix} = a^{-1} s_1 s_2^{-1} m_1 m_2^{-1}$, where

$$a = \begin{bmatrix} 1 & 1 \\ ik_a/\varepsilon_a & -ik_a/\varepsilon_a \end{bmatrix}, \tag{3}$$

$$s_1 = \begin{bmatrix} 1 & 1 \\ ik_s/\varepsilon_s & -ik_s/\varepsilon_s \end{bmatrix}, \tag{4}$$

$$s_2 = \begin{bmatrix} e^{ik_s D_s} & e^{-ik_s D_s} \\ ik_s e^{ik_s D_s}/\varepsilon_s & -ik_s e^{ik_s D_s}/\varepsilon_s \end{bmatrix}, \tag{5}$$

$$m_1 = \begin{bmatrix} 1 & 1 \\ ik_m/\varepsilon_m & -ik_m/\varepsilon_m \end{bmatrix}, \tag{6}$$

$$m_2 = \begin{bmatrix} e^{ik_m D_m} & e^{-ik_m D_m} \\ ik_m e^{ik_m D_m}/\varepsilon_m & -ik_m e^{ik_m D_m}/\varepsilon_m \end{bmatrix}, \tag{7}$$

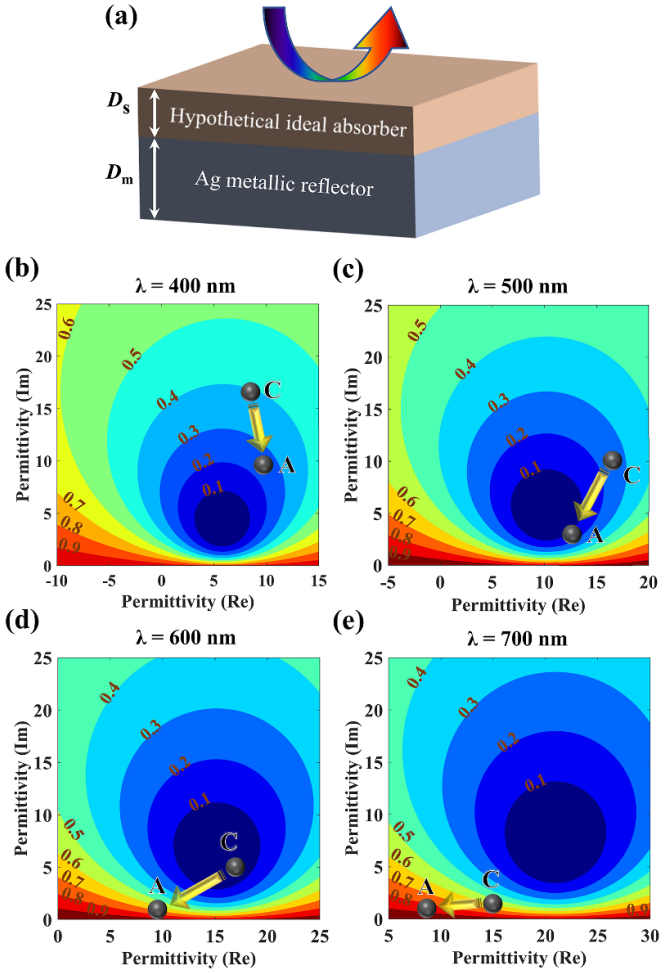

Figure 3. (a) Schematic representation of the planar design used for the TMM model and the corresponding reflection counterplots of the proposed planar design extracted for the TE polarization incident wave at four different wavelengths (b) 400 nm, (c) 500 nm, (d) 600 nm, and (e) 700 nm. The results are obtained for a 21 nm thick top hypothetical ideal material as a function of real and imaginary parts. In the figures, 'A' and 'C' denotes amorphous and crystalline states of Sb_2S_3, respectively.

and $k_{i=(a,s,m)} = \sqrt{\varepsilon_i \omega^2/c^2 - k_x^2}$ in which c is the speed of light, D_s is the thickness of HIA layer, and D_m is the bottom metallic layer thickness. Moreover, A_i, S_1, and M_1 are coefficients of the propagating waves along the $-y$-direction, and A_r, S_2, and M_2 are coefficients of the propagating waves along the $+y$-direction. The real and imaginary parts of the permittivity of a hypothetical ideal material can be calculated by using the formulas mentioned above. Considering the normal light incidence and the planar nature of the design, as shown in figure 3(a), the same response can be observed for the TE polarization. In a metal-HIA (where HIA thickness is fixed as D_s), the reflection contour plots are extracted at four different wavelength values of 400 nm, 500 nm, 600 nm, and 700 nm, as shown in figures 3(b)–(e). The permittivity values (both real and imaginary parts) of the top hypothetical absorbing layer should stay inside the $R = 0.1$ circle to satisfy the near-unity absorption requirement. Therefore, a planar hypothetical absorbing material on a reflector with the permittivity values located inside the centric dark blue circle can provide below 0.1 reflection. In contrast, the same patterned material may change and/or shift the resonances due to the change of n_{eff}. Since the FP phenomenon is the nature of the resonance wavelength of the proposed metasurface-based color filter for the TE polarization mode, a planar structure with an effective permittivity and thickness can be considered as an equivalent model of the nanograting design given in figure 1(b). Accordingly, the expectation is to have a near-unity absorption for the planar design at the wavelength of 500 nm and 600 nm for the amorphous and crystalline states of Sb_2S_3, respectively. Interpreting the 2D plots with permittivity values of amorphous (annotated as 'A') and crystalline ('C') Sb_2S_3 for the TE polarization (see figure 3 with filled circles) can validate our expectation that the near-unity absorption condition for 'A' and 'C' states should be satisfied at different wavelength values. This expectation is further investigated in figures 3(c) and (d), where the amorphous and crystalline states of Sb_2S_3 are located inside the $R = 0.1$ circle, respectively. Similar to figure 1(c), near unity absorption is obtained around 500 nm for the amorphous state, while the matching between the permittivity and ideal region occurs at 600 nm for the crystalline state.

3. A dynamically tunable photodetector design

3.1. Design, simulation, and results

In the second part of the present paper, an adaptive semiconductor-based metasurface photodetector is designed. For this aim, different from color filter design, a 5 nm thin embedded layer of Sb_2S_3 is added as a collection layer (see figure 4(a)). The proposed metasurface design enhances light–matter interaction in the Sb_2S_3 layer and leads to a larger density of electron–hole pairs. The generated carriers are separated using metallic Schottky contacts, as schematically explained in figure 4(b). We kept all the geometrical parameters as the optimized values of the first design and the only modified parameter is the thickness of the top Sb_2S_3 nanograting array $t = 15$ nm. However, the difference between photodetection and color filtering is the importance of light absorption in the semiconductor layer, which is essential for the efficient generation of electron–hole pairs. Therefore, to have a better qualitative comparison, the contributions of Sb_2S_3 layer and the nanograting structure to the overall absorption are obtained and shown in figure 4(c). The result obtained from this part is in good agreement with the overall absorption data (figure 1(c)), implying minimal parasitic absorption (inside the metal). This could also be seen in the absorption contour plots, depicted in the insets of figures 4(d)–(g). In the TM Amos. state, (shown in figure 4(d)), most of the incident light is absorbed within the planar Sb_2S_3 layer, while in the other three states, light is mainly harvested inside the grating design.

3.2. Photocurrent responsivity

To numerically investigate the electrical response of the photodetector, COMSOL Multiphysics, a finite-element-based

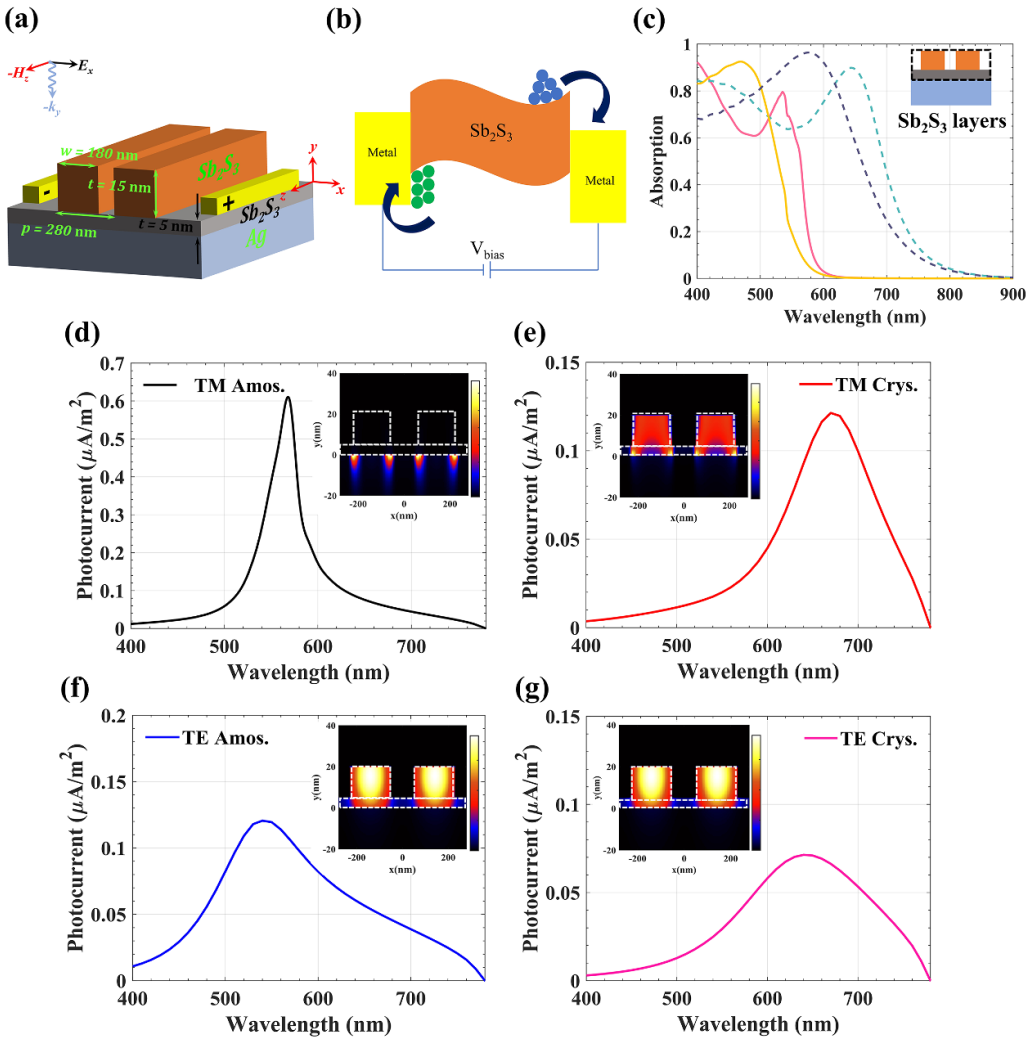

Figure 4. (a) The schematic representation of the proposed adaptive photodetection structure. The design now consists of a thin layer of Sb_2S_3 sandwiched between the top Sb_2S_3 nanograting array and the bottom reflector. (b) Representation of device operation under the visible incident light. (c) Contributions of Sb_2S_3 (planar and grating) layers on the overall absorption of the adaptive photodetection structure. The simulated photocurrent values of the adaptive photodetector as the function of wavelength for (d) TM Amos., (e) TM Crys., (f) TE Amos., and (g) TE Crys. states. The photocurrent responsivity of the proposed adaptive photodetection is obtained when the applied voltage is 2 V and the number of the grating is set to 10. The insets show the absorbed (dissipated) power densities of the metasurface-based photodetector at the resonance wavelengths, where the dashed white lines represent the Sb_2S_3 regions.

method solver, is utilized. COMSOL simulations are performed using the Optoelectronics interface, which couples the semiconductor and wave optics modules. So, photogeneration is added to the drift-diffusion equation via a term proportional to the electromagnetic fields. The bias voltage is applied using an ideal Schottky metal contact boundary condition, with the work function of the gold. It is observed that the photocurrent for the TM Amos. state can reach $0.60\,\mu A\,m^{-2}$ around 570 nm, while the photocurrent response for TM Crys. state is $0.12\,\mu A\,m^{-2}$ at 670 nm, as shown in figures 4(d) and (e), respectively. Furthermore, as shown in figures 4(f) and (g), the peak photocurrent responses are $0.12\,\mu A\,m^{-2}$ and $0.07\,\mu A\,m^{-2}$ for the TE Amos. and the TE Crys., states at the resonance wavelengths of 540 nm and 640 nm, respectively. The simulated results obtained from COMSOL Multiphysics software are in good agreement with the optical absorption of the proposed design, showing the efficient operation of this metasurface as an adaptive photodetector.

4. Conclusion

In conclusion, in the first part of the paper, we demonstrated the concept of dynamically tunable color filters in the visible range through the design of a semiconductor-based metasurface made of Sb_2S_3 nanograting on top of the continuous Ag layer. It is shown that the proposed metasurface design can exhibit four distinct operation states upon a change in the PCM phase and light polarization. The peak resonance wavelength for each of these states is located at different values, covering color filtering throughout the whole visible spectrum. The electric and magnetic field distributions

at the resonance wavelengths of the proposed metasurface absorber indicated that the formation of FP resonance is the dominant factor for the obtained resonance wavelengths for the TE polarization. In contrast, for TM polarization mode, surface plasmon resonances derive near-unity light absorption of the proposed structure. Later, in the second part of the paper, adaptive photodetection in the whole visible range is designed by integrating the ultrathin thickness (5 nm) of Sb_2S_3 layer into the structure. The proposed adaptive photodetection design now provides us the opportunity for unity light absorption in dimensions much smaller than the semiconductor diffusion length. Consequently, the collection efficiency of the photogenerated carriers is maximized. The adaptive optically thick and electrically thin design architectures open the door to designing efficient active optoelectronic and photonic devices.

Data availability statement

All data that support the findings of this study are included within the article (and any supplementary files).

Acknowledgment

E Ozbay acknowledges partial support from the Turkish Academy of Sciences (TUBA).

ORCID iDs

Ataollah Kalantari Osgouei https://orcid.org/0000-0002-0971-7687
Amir Ghobadi https://orcid.org/0000-0002-8146-0361
Bahram Khalichi https://orcid.org/0000-0002-9465-1044

References

[1] Kalantari Osgouei A, Hajian H, Khalichi B, Serebryannikov A E, Ghobadi A and Ozbay E 2021 Active tuning from narrowband to broadband absorbers using a sub-wavelength VO_2 embedded layer *Plasmonics* **16** 1013–21
[2] Landy N I, Sajuyigbe S, Mock J J, Smith D R and Padilla W J 2008 Perfect metamaterial absorber *Phys. Rev. Lett.* **100** 207402
[3] Khalichi B, Ghobadi A, Osgouei A K, Kocer H and Ozbay E 2021 A transparent all-dielectric multifunctional nanoantenna emitter compatible with thermal infrared and cooling scenarios *IEEE Access* **9** 98590–602
[4] Osgouei A K, Ghobadi A, Khalichi B and Ozbay E 2021 A spectrally selective gap surface-plasmon-based nanoantenna emitter compatible with multiple thermal infrared applications *J. Opt.* **23** 085001
[5] Osgouei A K, Hajian H, Serebryannikov A E and Ozbay E 2021 Hybrid indium tin oxide-Au metamaterial as a multiband bi-functional light absorber in the visible and near-infrared ranges *J. Appl. Phys.* **54** 275102
[6] Khalichi B, Ghobadi A, Osgouei A K and Ozbay E 2021 Diode like high-contrast asymmetric transmission of linearly polarized waves based on plasmon-tunneling effect coupling to electromagnetic radiation modes *J. Appl. Phys.* **54** 365102
[7] Menzel C, Helgert C, Rockstuhl C, Kley E B, Tünnermann A, Pertsch T and Lederer F 2010 Asymmetric transmission of linearly polarized light at optical metamaterials *Phys. Rev. Lett.* **104** 253902
[8] Smith D R, Pendry J B and Wiltshire M C 2004 Metamaterials and negative refractive index *Science* **305** 788–92
[9] Valentine J, Zhang S, Zentgraf T, Ulin-Avila E, Genov D A, Bartal G and Zhang X 2008 Three-dimensional optical metamaterial with a negative refractive index *Nature* **455** 376–9
[10] Kaschke J, Blume L, Wu L, Thiel M, Bade K, Yang Z and Wegener M 2015 A helical metamaterial for broadband circular polarization conversion *Adv. Opt. Mater.* **3** 1411–7
[11] Zhu H L, Cheung S W, Chung K L and Yuk T I 2013 Linear-to-circular polarization conversion using metasurface *IEEE Trans. Antennas Propag.* **61** 4615–23
[12] Qu Y, Li Q, Gong H, Du K, Bai S, Zhao D and Qiu M 2016 Spatially and spectrally resolved narrowband optical absorber based on 2D grating nanostructures on metallic films *Adv. Opt. Mater.* **4** 480–6
[13] Shen F, Kang Q, Wang J, Guo K, Zhou Q and Guo Z 2018 Dielectric metasurface-based high-efficiency mid-infrared optical filter *Nanomaterials* **8** 938
[14] Song S, Chen Q, Jin L and Sun F 2013 Great light absorption enhancement in a graphene photodetector integrated with a metamaterial perfect absorber *Nanoscale* **5** 9615–9
[15] Li W and Valentine J 2014 Metamaterial perfect absorber based hot electron photodetection *Nano Lett.* **14** 3510–4
[16] Wang Y, Sun T, Paudel T, Zhang Y, Ren Z and Kempa K 2012 Metamaterial-plasmonic absorber structure for high efficiency amorphous silicon solar cells *Nano Lett.* **12** 440–5
[17] Wu C, Neuner B III, John J, Milder A, Zollars B, Savoy S and Shvets G 2012 Metamaterial-based integrated plasmonic absorber/emitter for solar thermo-photovoltaic systems *J. Opt.* **14** 024005
[18] Krishna S 2005 Quantum dots-in-a-well infrared photodetectors *J. Phys. D: Appl. Phys.* **38** 2142
[19] Kishino K, Unlu M S, Chyi J I, Reed J, Arsenault L and Morkoc H 1991 Resonant cavity-enhanced (RCE) photodetectors *IEEE J. Quantum. Electron.* **27** 2025–34
[20] Koppens F H L, Mueller T, Avouris P, Ferrari A C, Vitiello M S and Polini M 2014 Photodetectors based on graphene, other two-dimensional materials and hybrid systems *Nat. Nanotechnol.* **9** 780–93
[21] Chamoli S K, Verma G, Singh S C and Guo C 2021 Phase change material based hot electron photodetection *Nanoscale* **13** 1311–7
[22] Kats M A, Sharma D, Lin J, Genevet P, Blanchard R, Yang Z and Capasso F 2012 Ultra-thin perfect absorber employing a tunable phase change material *Appl. Phys. Lett.* **101** 221101
[23] Luo H, Wang B, Wang E, Wang X, Sun Y, Li Q and Liu K 2019 Phase-transition modulated, high-performance dual-mode photodetectors based on WSe_2/VO_2 heterojunctions *Appl. Phys. Rev.* **6** 041407
[24] Guo Z, Yang X, Shen F, Zhou Q, Gao J and Guo K 2018 Active-tuning and polarization-independent absorber and sensor in the infrared region based on the phase change material of $Ge_2Sb_2Te_5$ (GST) *Sci. Rep.* **8** 1–8
[25] Liu H, Dong W, Wang H, Lu L, Ruan Q, Tan Y S and Yang J K 2020 Rewritable color nanoprints in antimony trisulfide films *Sci. Adv.* **6** eabb7171

[26] Delaney M, Zeimpekis I, Lawson D, Hewak D W and Muskens O L 2020 A new family of ultralow loss reversible phase-change materials for photonic integrated circuits: Sb_2S_3 and Sb_2Se_3 *Adv. Funct. Mater.* **30** 2002447
[27] Lumerical 2018 F D T D Solutions, Inc.
[28] COMSOL Multiphysics 1998 *Introduction to Comsol Multiphysics®* (Burlington, MA: COMSOL Multiphysics) (Accessed 9 February 2018) p 32
[29] Johnson P B and Christy R W 1972 Optical constants of the noble metals *Phys. Rev.* B **6** 4370
[30] Schanda J (ed) 2007 *Colorimetry: Understanding the CIE System* (New York: Wiley)
[31] Soydan M C, Ghobadi A, Yildirim D U, Duman E, Bek A, Erturk V B and Ozbay E 2020 Lithography-free random bismuth nanostructures for full solar spectrum harvesting and mid-infrared sensing *Adv. Opt. Mater.* **8** 1901203